Colloids and Surfaces A: Physicochemical and Engineering Aspects 702 (2024) 134943

Contents lists available at ScienceDirect

Colloids and Surfaces A: Physicochemical and Engineering Aspects

journal homepage: www.elsevier.com/locate/colsurfa

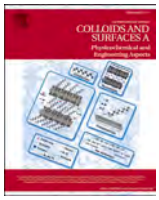

# Emulsions stability in weightlessness: Droplets size, droplets coalescence and phases spatial distribution

Angeliki P. Chondrou, Sotiris P. Evgenidis, Thodoris D. Karapantsios, Margaritis Kostoglou *

*Department of Chemical Technology and Industrial Chemistry, School of Chemistry, Aristotle University of Thessaloniki, University Box 116, Thessaloniki 541 24, Greece*

## HIGHLIGHTS

- Emulsification experiments are performed under microgravity conditions
- Droplet size distribution is affected by the emulsification parameters (e.g., oil volumetric fraction, stroke frequency)
- Coalescence of droplets is observed at different directions with no clear correlation with emulsification parameters
- Optically and electrically registered droplet sizes differ significantly due to differing measuring principles

## GRAPHICAL ABSTRACT

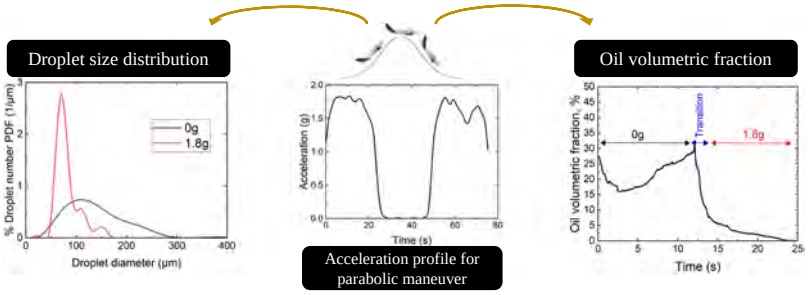


## ARTICLE INFO

*Keywords:*
Emulsion stability
Parabolic flights
Coalescence
High-speed imaging
High-resolution imaging
Electrical impedance spectroscopy

## ABSTRACT

This work presents experiments for the stability study of oil-in-water emulsions at varying gravity conditions. A key factor influencing emulsions stability is droplet size which can be assessed by several techniques employing different physical principles. Experiments are performed during the 79th Parabolic Flight Campaign of European Space Agency (October 2022). A pulsatile miniature emulsification device is used to produce emulsions in ~0 g conditions while using varying experimental parameters (oil volumetric fraction, surfactant concentration, pulsation frequency, number of strokes). The device resembles the Soft Matter Dynamics facility onboard the International Space Station whereas the examined parameters are also alike to Soft Matter Dynamics experiment. Optical measurements are employed to determine the droplet size distribution as well as, to observe coalescence events in the aqueous phase. Electrical measurements with a non-intrusive, on-line, impedance spectroscopy technique are carried out to track the evolution of oil volumetric fraction at the central region of the emulsification cell. As expected, in the absence of gravity, the buoyancy related phenomena are eliminated and, thus, phase gravitational separation between the two phases (creamy and aqueous) does not take place. Yet, the residual motion at the end of emulsification affects (a) the spatial homogeneity (distribution) of the two phases in the cell and (b) the capacity for coalescence of colliding droplets. In the absence of gravity, these two emulsion parameters are controlled solely by hydrodynamics and interfacial phenomena whereas on earth they are masked by buoyant phenomena. It is found that the oil fraction evolution curves resulting from electrical measurements are compatible with a bidisperse oil droplet size distribution. The characteristic sizes of the two droplet modes are estimated using theoretical arguments. Both the electrically volume-based determined droplet sizes and the number-based ones from high resolution image analysis are discussed in detail.

* Corresponding author.
*E-mail address:* kostoglu@chem.auth.gr (M. Kostoglou).

https://doi.org/10.1016/j.colsurfa.2024.134943
Received 26 April 2024; Received in revised form 1 July 2024; Accepted 28 July 2024
Available online 31 July 2024

## 1. Introduction

Emulsions are encountered in a great variety of industrial applications, e.g. foods, cosmetics, pharmaceuticals. They are also employed in the petroleum industry and oil recovery processes [1–4]. Emulsions are colloidal multiphase systems consisting of two, partially or completely, immiscible liquids (e.g. oil and water) where the first liquid is embedded (dispersed phase) into the second liquid (continuous phase) in the form of droplets [5]. Essentially, there are three types of emulsions based on the nature of the dispersed phase which are oil-in-water (O/W), water-in-oil (W/O) and multiple emulsions that can be considered as emulsions in emulsions (W/O/W or O/W/O) [6]. The emulsification process, usually by shearing or agitation, requires a considerable amount of mechanical energy to produce droplets. However, this system is thermodynamically unstable and long-term stability can be achieved only by the addition of a third component, the emulsifier which is often a surfactant. The latter decreases the interfacial tension of the oil-water system, modifies its interfacial rheology and, thus, facilitates droplet break-up and prevents droplets coalescence [7,8].

Emulsion properties that strongly affect the coalescence rate of droplets and as a consequence are linked to their stability may be related either with the materials that compose the emulsion (nature of the interfacial film, droplet charge, viscosity of the continuous phase, phase volume ratio) or to those delimited by the emulsification process (droplet size distribution) [9]. Different mechanisms contribute to emulsion destabilization during their storage in vessels. The gravity driven processes of creaming and sedimentation (due to density difference between the two phases) are not always considered as serious destabilization processes since they do not result to increase of droplet size. On the contrary, the interface driven processes of coalescence (due to thinning and disruption of the liquid film between droplets), aggregation (formation of droplets clusters) and Ostwald ripening (due to size depended solubility of dispersed phase in the continuous one) lead to droplet size increase and, finally, the system separates into the two initial immiscible bulk liquids (phase segregation) [10,11].

It must be stressed that the gravity driven processes facilitate the interface driven ones. After the end of the emulsification process the emulsion consists of two different phases, the creamy (oily) and the aqueous. Typically, each of these two phases constitutes an emulsion since they both contain oil and water. The creamy phase holds a high oil volume fraction while the aqueous phase holds a much smaller one. In the presence of gravity (in either normal or high gravity conditions) the rapid separation (creaming or sedimentation) of the aqueous phase from the creamy phase is triggered. Motion of droplets as well as droplets interactions evolve rapidly, and the mechanisms of coalescence and aggregation take place too fast. In order to investigate thoroughly the rapid interface driven emulsion destabilization mechanisms, the respective gravity driven ones have to be eliminated and this can be achieved at a low gravity environment. During emulsification the effect of gravity seems to be quite limited since the emulsification itself is a complex intense energy process including droplet deformation, coalescence and/or breakage [12]. However, after the end of the emulsification process and in the absence of gravity, phase separation does not take place, the motion of droplets and droplets interactions get slower and as a result, coalescence and aggregation can be studied in-depth.

So far, micro-gravity experiments concerning surfactant adsorption dynamics, droplets interactions and interfacial film destabilization as well as, evolution of droplet size distribution of produced emulsions have been designed to be performed on-board the International Space Station (ISS) [13,14]. The ISS offers the capability to perform experiments over an extended period of time in weightlessness (from hours to years). Parabolic flights offer access to micro-gravity conditions as well, where a specially modified airplane executes a series of maneuvers called parabolas. Each parabola provides a short micro-gravity period of ~22 s and a key feature is that immediately prior and following to the short period of micro-gravity conditions during each parabola there are also two periods of increased gravity (~1.5–1.8 g).

As mentioned before, droplet size distribution strongly affects emulsion stability. An emulsion becomes more stable for narrower droplet size distribution. Conventionally, droplet size distributions of emulsions are assessed by microscopy techniques (i.e. optical, confocal or electron microscopy), light scattering techniques (i.e. dynamic light scattering or static light scattering), diffusing wave spectroscopy (DWS), electroacoustic techniques (i.e. ultrasonic, dielectric spectroscopy) or nuclear magnetic resonance [15–17]. The majority of these methods are characterized by the fact that either they provide information of droplet sizes only from places where there is visual access (measuring a small portion of total emulsion) or they are subjected to a sampling mechanism (external forces insertion which may disturb the initial distribution). It is worthy to mention that DWS is a non-invasive and relatively simple spectroscopic technique which allows real-time monitoring of the whole sample without subjecting external forces. However, DWS provides information regarding the average droplet size and not the entire droplet size distribution [17–19]. Additionally, there is another non-conventional tempting option which employs non-intrusively, and across the whole emulsion volume, on-line electrical conductance measurements to estimate dispersed phase fraction. This technique is based on the conductivity difference of the two phases (water is conductive while oil droplets are non-conductive) [20]. Another significant issue that arises is that the above mentioned techniques rely on different measuring principles and as a consequence, some of them provide information based on number intensity (each droplet has equal contribution to the final distribution) whereas other provide distributions based on volume intensity (the smallest droplets are overlooked due to their negligible volume contribution). This implies that results from two techniques based on different physical principles are complementary to each other.

A previously developed experimental setup by Chondrou et al. [21], complying with the safety regulations applying to Parabolic Flight Campaigns (PFC) of the European Space Agency (ESA), is employed with the aim to exploit the different gravity conditions for the stability evaluation of emulsions. Identification of critical parameters during present experiments allowed the optimization of Soft Matter Dynamics (SMD) experiment on-board the ISS as well as, the interpretation of generated results. The emulsification process takes place during micro-gravity conditions and the purpose here is to observe phenomena occurring right after emulsification (during micro-gravity period and at the beginning of the hyper-gravity one). Stability of emulsions is registered by monitoring droplet sizes, the distribution of which is considered as good initial indicator of stability; a further indicator is the interfacial viscoelastic properties of droplets but this aspect is beyond the scope of the present study. Since optical images capture only a small portion of the test cell volume, electrical measurements are employed to independently estimate droplets sizes from the variation of oil volumetric fraction during the hyper gravity period following the microgravity one, in a large portion of the test cell volume. The theoretical background and methodology for estimating droplet sizes from the evolution of the measured electrical signals is described in detail.

## 2. Materials and methods

Both the experimental device and procedure have been presented in detail in our previous work [21] and thus only some essential elements are repeated here. The experimental device, built in compliance with the safety regulations applying to ESA parabolic flights (Novespace, 2023), is divided into three parts, two experimental racks and one separate baseplate (Fig. 1**a**). Each rack is composed of the primary structure and the payload. The 1st rack's payload consists of the emulsification unit (including a sliding case that houses five exchangeable test cells in a line), the optical and electrical diagnostics. The corresponding payload for the 2nd rack contains solely a storage unit that secures 5 additional sliding cases, each one accommodating five test cells (in total six

drawers housing thirty experimental cells). The baseplate standing separately between the two racks houses the electrical control panel of the device as well as the processor of the high speed camera.

The core of the experimental device is the emulsification unit (Fig. 1**b**). The unit includes the aluminum frame in which the motor unit (stepper motor and rack-pinion gear system) and a test cell case, that supports five exchangeable experimental cells, are integrated. The test cell case is placed on a carrier that facilitates its displacement at five fixed positions which allows a different experimental cell to be used in each parabola of the sequence of 5-parabolas in a set (see below). The emulsification process takes place inside the aluminum experimental cell (Fig. 1**c**) with dimensions 12 ×14 x 26 mm. Two of the parallel cell walls are made of glass offering ports for optical recordings and lighting. The two remaining walls are made of Plexiglas. Non-intrusive, circular (edge of rods) electrodes are flush-mounted to the parallel Plexiglas walls for performing electrical measurements. A cylindrical piston is integrated to the lid of the cell. A thin aluminum plate is fixed at the tip of the piston. Almost the entire cross-section of the cell is scavenged by the plate of the piston. During emulsification, the piston moves periodically and repeatedly up and down along the perpendicular axis mixing the two phases and as a result, produces, deforms and breaks up oil droplets. The piston motion is guided by a stepper motor through the rack-pinion gear system that converts its rotary movement to the linear motion of the piston. The lid of the cell has also two communication ports for feeding the test liquids into the cell.

Dynamic behavior and stability study of the produced emulsions is recorded by means of advanced optical and electrical diagnostics. The optical diagnostics unit (Fig. 2**a**) incorporates two cameras (high speed and DSLR digital camera) combined with a cube beam splitter, which enables simultaneous optical recording of the emulsion behavior by these two cameras, as well as LED backlight to provide the necessary illumination. The Photron Multi FASTCAM high speed is used to investigate droplet-droplet interactions (e.g., coalescence events). The CANON EOS 70D digital camera is utilized to capture successive high resolution images of the produced emulsion for the determination of droplet size distribution evolution under both micro-gravity and hyper-gravity conditions. Image analysis by the custom software BubbleSEdit, which is capable of detecting even strongly overlapping droplets under varying illumination conditions, provides the evolution of droplet size distribution with time and gravity [22].

An EU patented I-VED electrical impedance spectroscopy technique (*EP 3 005 942 A1, 2016*), originally developed for the detection of bubbles in astronauts bloodstream during Decompression Sickness, is employed for the registration of oil volumetric fraction exploiting the gravity dependent separation of oil droplets from the aqueous phase during the hyper-gravity period following microgravity conditions in a parabola. The I-VED electrical diagnostic, thus, enables to investigate the evolution of oil volumetric fraction as a function of time and gravity after the end of emulsification. The present technique has been successfully tested in different two-phase systems, as well as in a few in-vivo studies [23–31]. I-VED performs electrical impedance measurements through the two rod electrodes, which are in contact with the emulsion under study (Fig. 2**b**). A sinusoidal voltage signal with an amplitude of 2 Vp-p and a frequency of 25 kHz that excites electrically the two-phase system is applied and a 20-bit data acquisition card records the electrical signal with a sampling frequency of 192 kHz. Frequency scanning showed that an excitation frequency of 25 kHz provides the lowest phase shift (less than 1°) and is the optimum value in terms of effective electrodes polarization and capacitance contribution elimination. The signal undergoes conditioning and treatment and the final output of data reduction is an electrical impedance time-series which is transformed to oil volumetric fraction time-series employing the appropriate model (e.g Maxwell or Bruggeman) [23].

The experiments are conducted in October 2022 during the ESA 79th PFC including 3 daily flights on board an Airbus A310 Zero-G airplane operated by Novespace. Each flight contains 31 parabolic maneuvers (parabolas): an initial trial one for newcomers onboard and then 30 regular ones. The parabolic maneuver total duration is ~80 s and the duration of weightlessness is ~22 s. The maneuver includes three different phases: a) entry phase (vertical load factor of ~1.8 g / ~24 s),

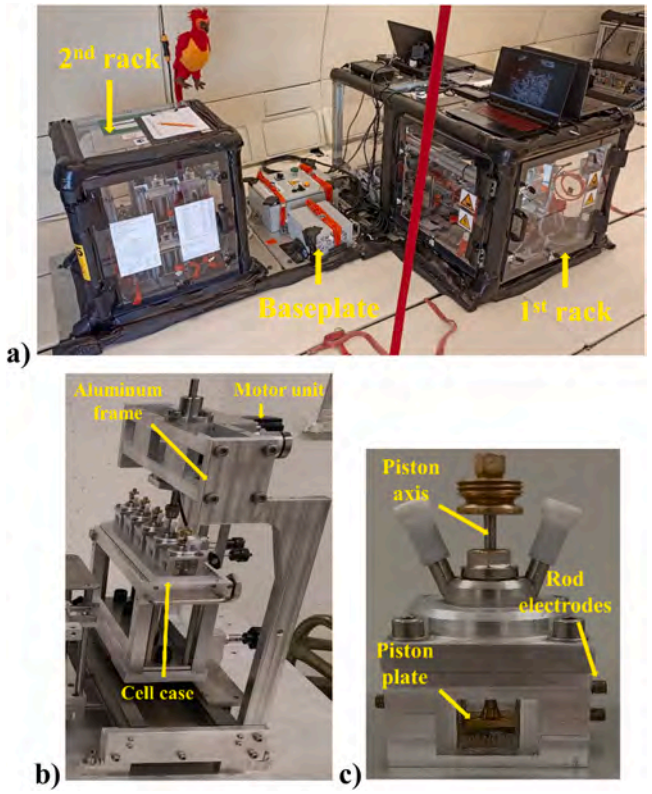


**Fig. 1. a)** The experimental device, **b)** The emulsification unit and **c)** The experimental cell.

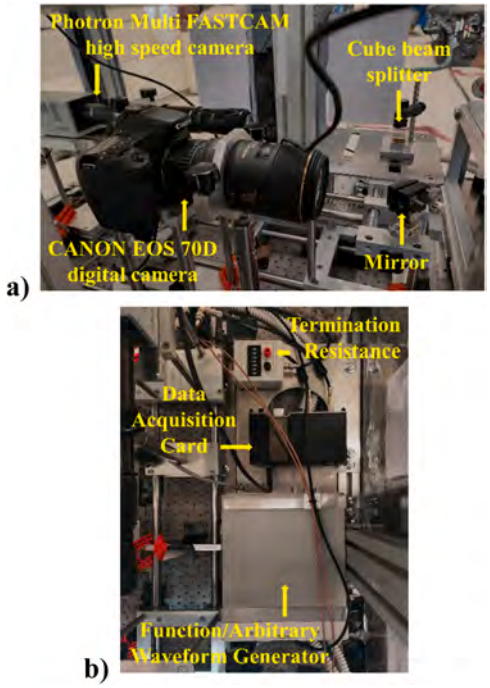


**Fig. 2. a)** The optical diagnostics unit (side view) and **b)** The electrical diagnostics unit (top view).

b) injection (micro-gravity) phase (vertical load factor ~0 g / ~22 s) and c) exit phase (vertical load factor ~1.8 g / ~24 s). There are two short (~5 s) transition phases between the aforementioned three main phases. The acceleration α profile of all parabolas is recorded during the flight (Fig. 3). The 30 regular parabolas are split in 6 sets of 5 parabolas sequence per set. Each one of these sets is interrupted by a 5–8 min break.

All 30 pre-cleaned experimental cells are filled with the appropriate liquids (aqueous and organic phase) by using a feeding routine before each experimental day of the PFC and then, are placed and secured in the storage unit on-board the aircraft. After the take-off and before the first parabola, tuning of all devices is performed and the 1st cell case is placed in the emulsification unit making all the necessary connections. The emulsification process takes place normally during ~0 g conditions, but it may start earlier (i.e. in the entry phase, ~1.8 g) in the case it is planned to last too long (more than 10 s). The optical and electrical measurements are employed during ~0 g and the following ~1.8 g conditions. Despite the short duration (~22 s), the micro-gravity conditions evolving per parabola allow the investigation of droplet interactions (coalescence phenomenon) after the end of emulsification which is not possible on earth. In the corresponding experiments onboard ISS these phenomena will be studied for an extended period of time. In the ninety seconds break between two successive parabolas (~1 g conditions) the case is properly moved to the next experimental cell and this procedure is followed for five consecutive experiments (each at a different test cell of a cell case) and at the end of the first set of five parabolas, the first cell case is replaced by another one consisting of other five experimental cells.

Materials used for the preparation of oil-in-water emulsions are millipore water (0.05μS/cm, Direct-Q® 3UV), MCT oil (IOI Oleo Chemical) and Nikkol BL-21 (Nikko Chemicals, water soluble, nonionic surfactant, CMC: $2.5\bullet10^{-4}$ M) surfactant as emulsifier. Aqueous solutions of Nikkol BL-21 are employed as the aqueous phase and MCT oil is applied as the organic phase of emulsions tested onboard the aircraft. NaCl is also added in the aqueous solution of surfactant for conductivity regulation. After salt dissolution the electrical conductivity of the aqueous phase is ~130 μS/cm. It must be noted, though, that the present electrical technique is fully functional at even much lower values of conductivity. Conductivity regulation in the present experiments is necessary to ensure a standard conductivity value for all experiments. The increase of conductivity of the aqueous phase allows the electrical noise to signal ratio reduction. The four parameters examined during micro-gravity experiments are: a) oil volumetric fraction (from 0.05 to 0.20), surfactant Nikkol BL-21 concentration (from 0 to $2\bullet10^{-4}$ M), c) pulsation stroke frequency (10 and 15 Hz) and d) number of strokes (from 9 to 90).

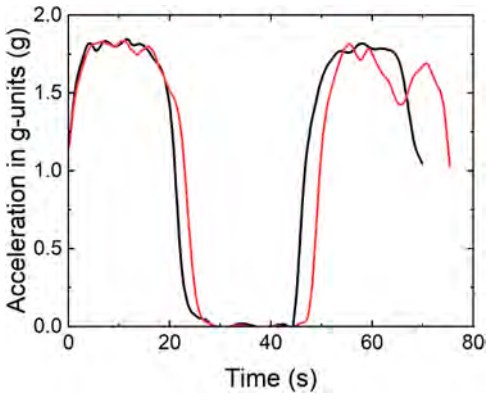


**Fig. 3.** Acceleration profile of two different parabolas of the 79th ESA PFC.

## 3. Results and discussion

### 3.1. Optical measurements

An important question is the recognition of the droplet breakage mechanism. In a previous work [32], the cell flow field was analysed in terms of fluid shear for a different physical system. However in the present work the viscosity ratio between oil and water is larger than 30. So according to [33] the pure shearing cannot be the breakage mechanism. It appears that breakage occurs due to extensional flow during the entrance of the fluid in the gap between cell and piston.

As already mentioned, both optical and electrical measurements are employed throughout all parabolic maneuvers. Indicative high resolution images of oil droplets during emulsification experiments at different time intervals are presented first (Fig. 4**a**). The camera is configured to automatically take one a picture every 5 s starting before emulsification and ending in the hypergravity exit phase of the maneuver. The three pictures at t = 0 s (immediately after the end of the emulsification process), 5 s and 10 s are taken during micro-gravity conditions while the next two, t = 15 s and 20 s are captured during hyper-gravity conditions in synchronization with the acceleration profile during each parabola. During the present experiments, all droplets shown in each image are circled one by one (~200–300 oil droplets). Droplets larger than 400 μm have not been taken into account since they are big enough to be considered as emulsion droplets and they are rare enough to modify stochastically the derived size distributions.

The radii of the measured droplets are exported from the software and after some mathematical calculations the droplet size distribution is obtained and presented in graphs of the % droplet number probability density function (PDF) versus droplet diameter. Fig. 4**b** shows the droplet size evolution in terms of number PDF for an emulsion examined in the present study. During micro-gravity conditions (t = 0, 5 and 10 s) a broad droplet size distribution (~30–350 μm) is observed while during hyper-gravity conditions (t = 15 and 20 s) the droplet size distribution becomes narrower (and accordingly sharper) towards smaller sizes (~30–150 μm). This proves that during hyper-gravity conditions, buoyancy triggers the rapid separation of creamy phase from the aqueous phase during which arge oil droplets move faster to the top of the cell than the smaller ones. Moreover, during the entire micro-gravity period (t = 0, 5 and 10 s) the emulsion is characterized by similar droplet size distributions indicating the absence of severe organized droplet motion leading to coalescence (buoyancy related phenomena are eliminated). As a result, more or less the same droplets are noticed and circled in the three successive images. Small discrepancies are observed due to either the remaining motion of droplets after the end of pulsation or the transition from injection phase to the exit phase of the maneuver. In addition, the corresponding number-based droplet average diameter evolution based on image analysis is presented in Fig. 4**c**. As expected, and in compliance with the droplet size distribution, the number-based average diameter $d_{av}$ remains almost constant during micro-gravity conditions (~130 – 150 μm) and decreases at hyper-gravity conditions (~70 – 80 μm).

The comparison between the number-based droplet average diameters follows (Figs. 5, 6). The first examined parameter is the oil volumetric fraction while the effect of surfactant concentration is studied next. Two different oil volumetric fractions are used for the preparation of emulsions, i.e. 0.05 and 0.1 (Fig. 5**a**) and two different surfactant concentrations, i.e. $10^{-5}$ and $2\bullet10^{-4}$ M (Fig. 5**b**). It seems that the average diameter decreases as the oil volumetric fraction decreases or the surfactant concentration increases. Surfactant concentration primarily affects the interfacial tension of the oil-water system. As the surfactant concentration increases the interfacial tension decreases causing a reduction in droplet size. In addition, the surfactant layer serves as a barrier to coalescence leading also to reduction in droplet size. Moreover, the dispersed phase volumetric fraction strongly affects droplet size. As the volume of the dispersed phase increases, the

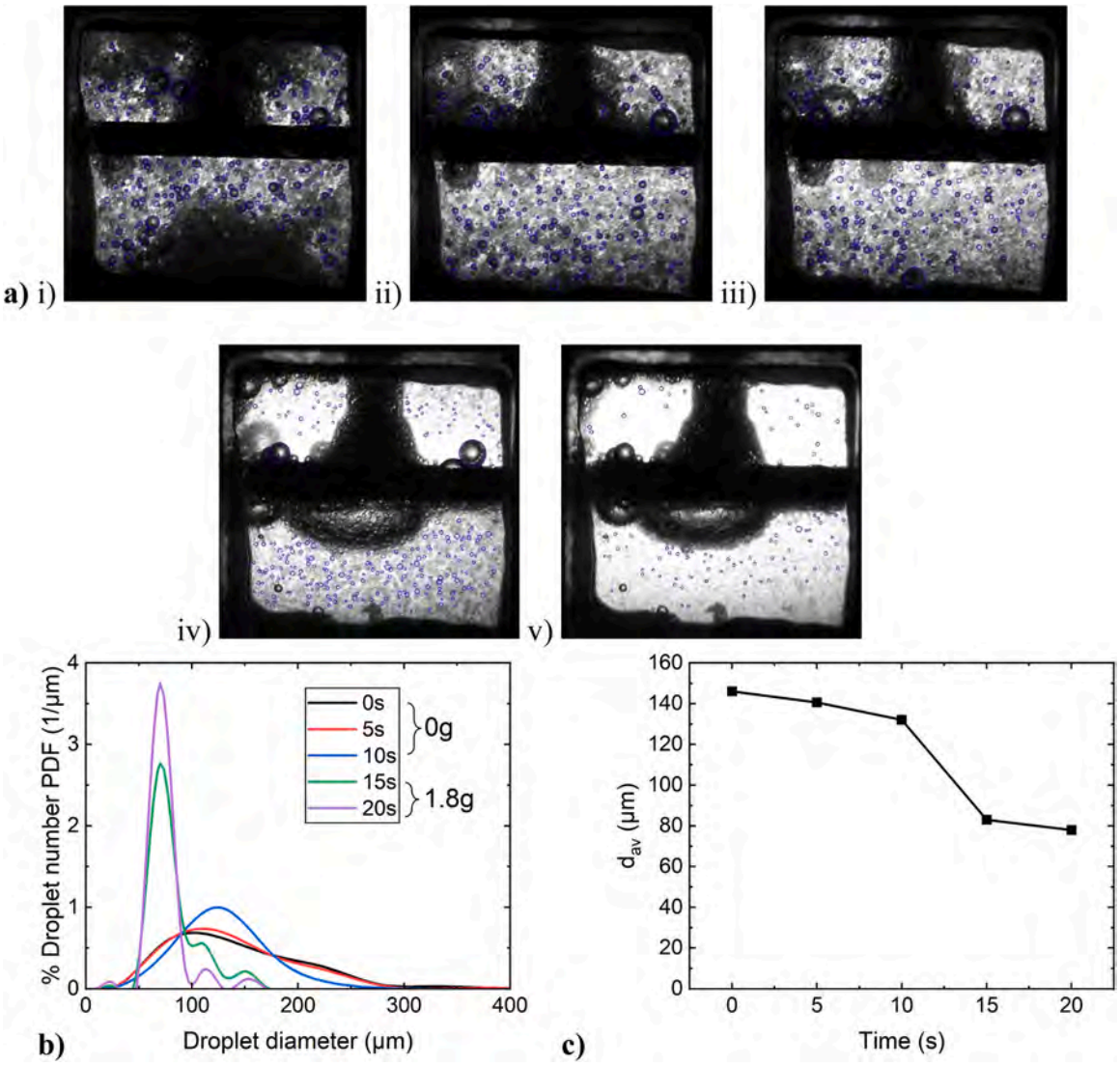


**Fig. 4.** **a)** Oil droplet images at i) t=0 s, ii) t=5 s, iii) t=10 s, iv) t=15 s, v) t=20 s after the end of emulsification, **b)** Droplet size distributions evolution as a function of time and gravity and **c)** Number-based droplet average diameter as a function of time and gravity (see legend in Fig. 4**b**) of emulsion (φ=0.1, $C_{surf}$=2•$10^{-4}$ M, f=10 Hz, No of strokes=18).

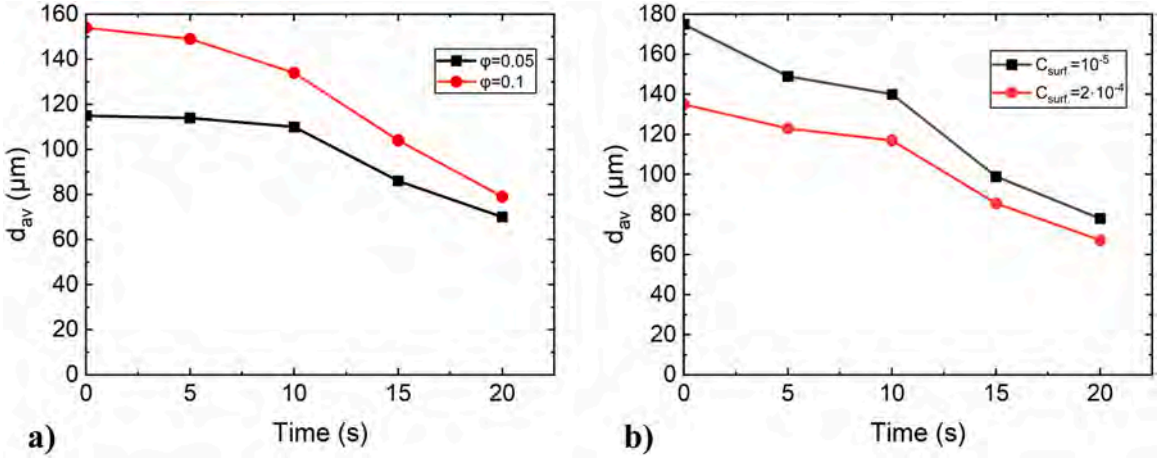


**Fig. 5.** Number-based droplet average diameter of emulsions for different **a)** oil volumetric fractions (φ) ($C_{surf.}$=$10^{-5}$ M, f=10 Hz, No of strokes=90) and **b)** surfactant concentrations ($C_{surf.}$) (φ=0.1, f=10 Hz, No of strokes=63).

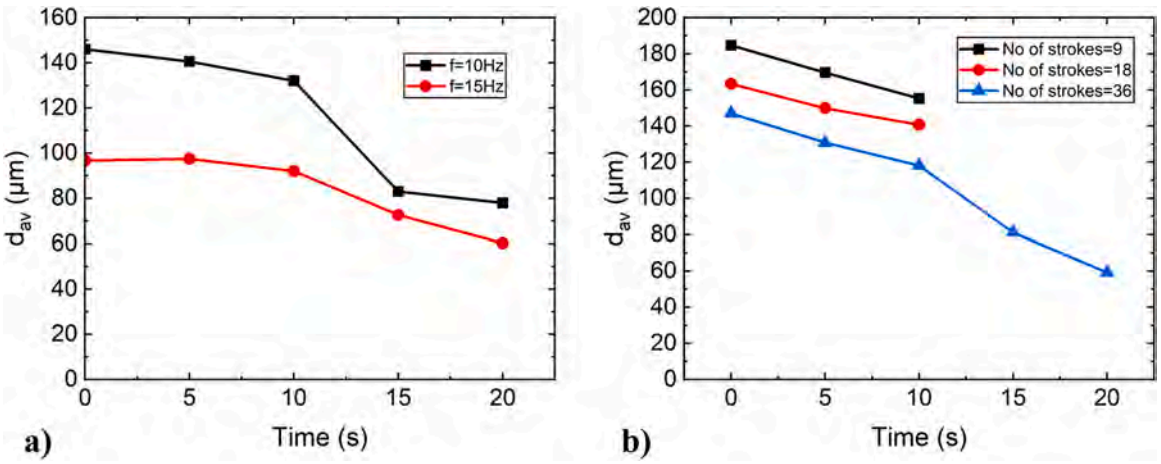


**Fig. 6.** Number-based droplet average diameter of emulsions for different **a)** pulsation stroke frequencies (f) (φ=0.1, $C_{surf.}$=2•$10^{-4}$ M, No of strokes=18) and **b)** number of strokes (φ=0.05, $C_{surf.}$=$10^{-5}$ M, f=10 Hz).

turbulent shear stresses in the flow field are dampened leading to increased droplet size. An additional reason for the increase of droplet size with oil fraction is the increase of droplet collisions which lead to coalescence during emulsification.

Next, the influence of the pulsation stroke frequency and the number of strokes are examined. Two different pulsation stroke frequencies, 10

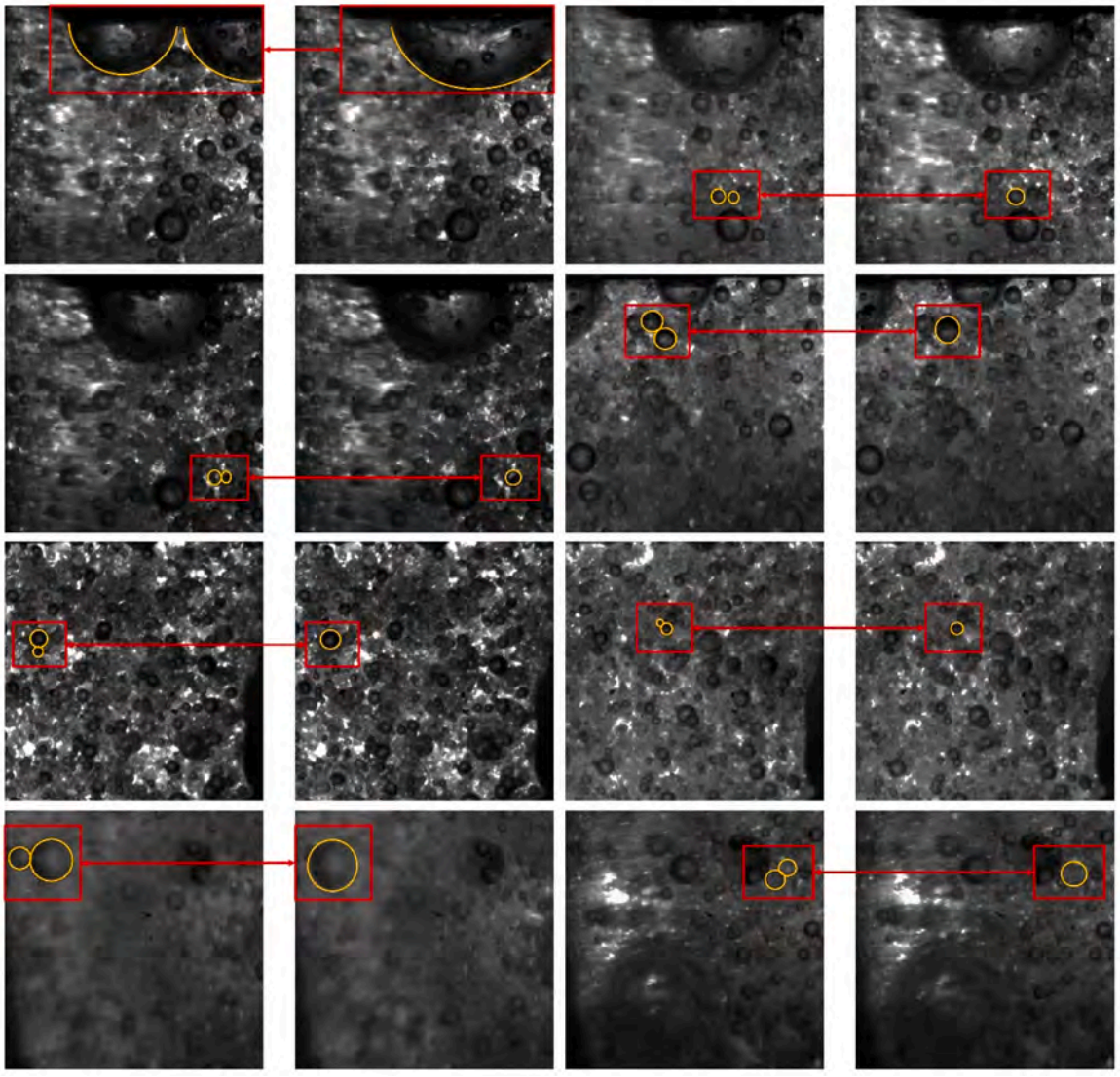

**Fig. 7.** Indicative directly evidenced coalescence events in the aqueous phase of emulsion (φ=0.1, $C_{surf}$=$10^{-5}$ M, f=15 Hz, No of strokes=18).

and 15 Hz at 18 strokes are employed (Fig. 6**a**), followed by three different numbers of strokes, 9, 18 and 36 at a pulsation stroke frequency of 10 Hz (Fig. 6**b**). In the abovementioned range of these parameters, it is observed that the number-based average diameter decreases as both the pulsation stroke frequency and the number of strokes increases. These emulsification parameters play an important role on droplet size in accordance with similar findings reported by Kori et al. [34], Naeeni and Pakzad [35] and Suli et al. [36]. It is noteworthy that in the cases of 9 and 18 strokes (Fig. 6**b**) the droplet size distributions during hyper-gravity conditions could not be generated. All droplets have moved rapidly to the top of the cell after the transition to the exit phase and there are no remaining droplets to be analyzed in the pictures. This indicates a bigger number of large droplets in the produced emulsion and the absence of smaller ones.

As already mentioned, in the present experiments emulsification takes place at micro-gravity conditions. Phase separation between the creamy phase (high oil volume fraction) and the aqueous phase (low oil volume fraction) does not take place after the end of pulsation. Analysis of the videos taken by the high-speed camera allows observation of different coalescence events during micro-gravity conditions. All coalescence events are observed in the aqueous phase where the residual motion of the piston periodical movement leads to oil droplets collisions and consequently to merging. When two oil droplets are in contact, the liquid film between them ruptures and the coalesced droplet instantaneously obtains a spherical shape driven by capillarity.

Based on video analysis, coalescence events can be characterized as directly evidenced and indirectly evidenced events. Indirectly evidenced classification refers to cases in which the one droplet is clearly observed while the other is hidden at the back of the first. When these droplets are in contact, then the coalescence phenomenon may take place and, if so, the clearly observed new born droplet seems to bounce instantaneously. Indicative directly evidenced coalescence events in the aqueous phase are shown in Fig. 7. In this case, the two droplets that coalesce are clearly seen to be next to each other. It is noticed that two droplets of either the same or different size is possible to merge to a single droplet. Furthermore, droplet coalescence may happen at different directions (vertically, horizontally and diagonally), as has been also noticed for the case of coalesced bubbles [37]. Because of the limited number of experiments during a parabolic flight campaign it was not possible to tell if there are different coalescence characteristics when varying the experimental parameters (oil fraction, surfactant concentration, pulsation frequency, number of strokes).

### 3.2. Electrical measurements

I-VED measurements capture with high sensitivity the variation of emulsion electrical resistance during the total duration of a parabolic maneuver. Fig. 8**a** presents the evolution of electrical resistance during the periodical movement of the piston with a frequency of 15 Hz for 1 s. Thirty intense signal peaks can be clearly noticed in 1 s, corresponding to two passes (downwards/upwards) of the piston plate per stroke in front of the measuring electrodes for the applied pulsation frequency.

In Fig. 8**b** the I-VED signal starting immediately after the end of emulsification/pulsation (t=0 s) is presented. It is reminded that emulsification/pulsation ends within the microgravity phase. The aqueous phase is the conductive phase, while the oil phase is the non-conductive

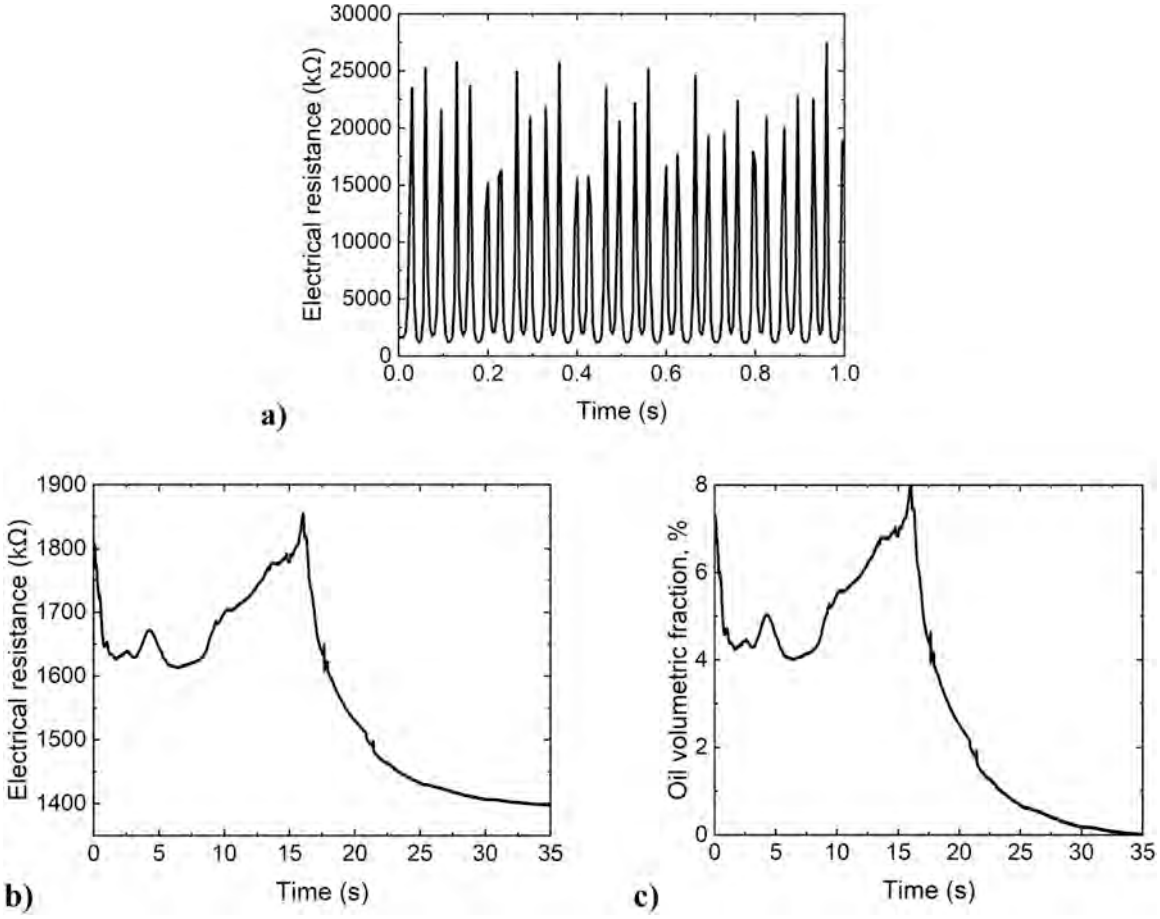


**Fig. 8.** Evolution of **a)** electrical resistance during the periodical movement of the piston with a pulsation stroke frequency of 15 Hz for 1 s, **b)** electrical resistance as a function of time during phase separation of an emulsion at different gravity conditions (for t<~16 s microgravity phase; for t>~16 s hypergravity phase) and **c)** oil volumetric fraction as a function of time during phase separation of an emulsion (φ=0.05, $C_{surf}=10^{-5}$ M, f=15 Hz, No of strokes=18).

one. There are two distinct regions in the curve. The first region refers to ~0 g conditions where the electrical resistance varies in an arbitrary manner because of the residual liquid motion after the end of pulsation. The second region occurs at ~1.8 g gravity conditions where the electrical resistance decreases progressively as oil droplets ascend forming a cream at the top of the cell, leaving the aqueous phase at the bottom. In this second hyper-gravity region the rising velocity of droplets determines the slope of the curves. The change in resistance of the emulsion is translated into change of oil volumetric fraction (Fig. 8**c**) via the Bruggeman equation (Eq. 1), which is suitable for random dispersions of spherical non-conducting particles [31]:

$$K_m = \frac{R_0}{R} = (1-\varphi)^{3/2} \quad (1)$$

where $K_m$ is the normalized resistance, $R_0$ is the resistance of the aqueous phase, R is the resistance of the emulsion (evolving with time) and φ is the oil volumetric fraction.

It must be stressed that the Bruggeman relation (like all other similar expressions) refers to a fully homogeneous dispersion of droplets inside a continuous phase. In our experiments, at the end of pulsation there is indeed an appreciable degree of dispersion of oil droplets in the aqueous phase but clearly this is far from ideal, that is, the dispersion is not fully homogeneous. Moreover, the residual motion of both liquids, because of the prior pulsation, agitates further the two liquids in an arbitrary manner sometimes increasing and sometimes decreasing the homogeneity of the dispersion. However, it appears that the time-averaged value of oil fraction during the micro-gravity region equals the value determined by the proportion of the two liquids. This indicates that, on the average only mild deviations from homogeneity appear, rendering feasible the use of Bruggeman law to derive approximate spatially averaged, instantaneous oil fraction.

Finally, the oil volumetric fraction evolution of emulsions with different values of the examined parameters (oil volumetric fraction, surfactant concentration, pulsation stroke frequency, number of strokes) is displayed (Figs. 9, 10). In the first region of the signals (~0 g conditions) fluctuations in the value of the electrical resistance are observed. These fluctuations are due to the residual motion after pulsation of the entire liquid volume in the experimental cell which makes oil droplets move in and out the measuring region between the rod electrodes. Furthermore, the two distinct major slopes observed in the second region of the signals (~1.8 g conditions), indicate that the droplet size distribution can be approximated by a bidispersed distribution rather than by a monodispersed one. The first steep slope corresponds to large droplets (fast reduction of oil volumetric fraction) whereas the second more gradual slope corresponds to smaller ones (slower reduction of oil volumetric fraction). A more detailed analysis of the oil volumetric fraction evolution curves is described in the next section.

## 4. Analysis of oil fraction evolution curves

A first observation is that the hyper-gravity leads always to a zero volume fraction of the oil between electrodes. This implies that the volume fraction of the small droplets whose motion is dominated by Brownian (diffusion) contributions, is negligibly small. The basic aspect determining the transition of the electrical resistance from a measurable finite oil fraction value to a value that indicates the absence of oil is the motion of droplets promoted by the induced buoyant acceleration. Before the onset of the induced acceleration, resistance fluctuations around the value that corresponds to the nominal oil fractions are only observed. These fluctuations are due to the residual motion of the liquid in the cell and the motion of the oil droplets in and out of the region between the electrodes. It is noticed that the broad size distribution of droplets enhances such fluctuations. From the above discussion appears that the droplet velocity is essential in determining the electrical resistance evolution. For this reason, an attempt is made to evaluate oil droplet velocities subjected to a varying induced acceleration. The transient character of the induced acceleration suggests starting from the transient equation of the droplet motion. The history of the corresponding equation dates back to Boussinesq and Basset [38] and was continued by Tchen [39] among many other authors that worked on it [40]. The basic equation refers to zero droplet Reynolds number. Several empirical extensions of the analysis have been suggested to account for a finite droplet Reynolds number [41]. The nonlinearity of the problem does not allow an explicit equation in this case, so an empirical treatment of the original equation is necessary. The governing equation for the droplet velocity evolution (Eq. 2) is presented as [42]:

$$\left(\rho + C\rho_f\right)\frac{dV}{dt} = \left(\rho_f - \rho\right)\alpha - \frac{3\rho}{8R}C_D U^2 \quad (2)$$

The first term denotes the accumulation of momentum, the second denotes the buoyancy force and the third the drag force. The velocity U is the relative velocity between a droplet and water and it may be different than the droplet velocity V. The Basset or history term has been ignored in the above equation since it is considered to be much smaller than the other terms. The coefficient C is the virtual mass coefficient. The virtual mass $\rho+C\rho_f$ of the droplet emerges from the fact that any motion of the droplet has to put into motion a quantity of water around the droplet. The inviscid limit value C=1/2 is assumed here since is the most frequent one used in literature [43]. The coefficient $C_D$ is the drag

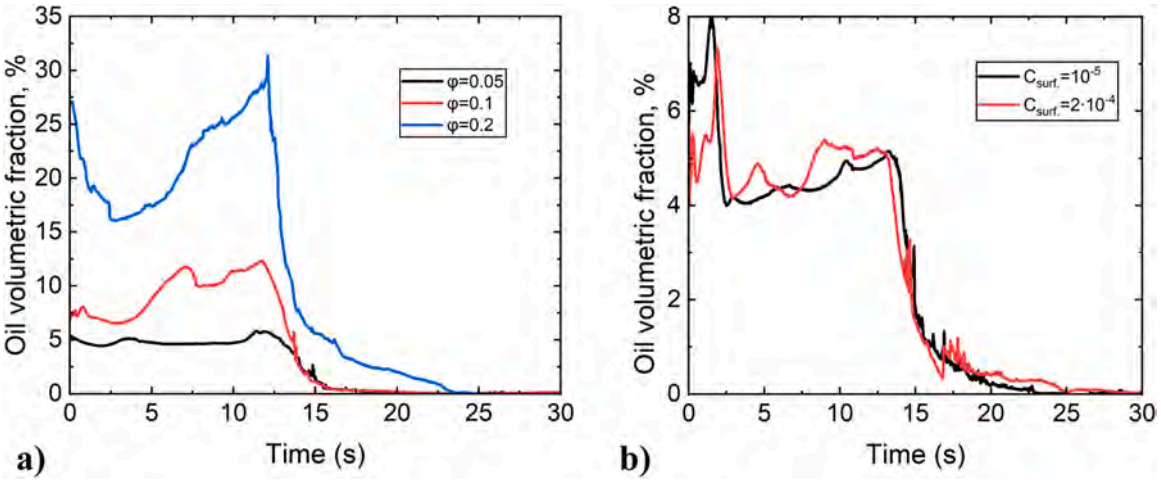


**Fig. 9.** Oil volumetric fraction evolution as a function of time and gravity during phase separation of emulsions with different **a)** oil volumetric fractions (φ) ($C_{surf.}$=2•10$^{-4}$ M, f=15 Hz, No of strokes=36) and **b)** surfactant concentrations ($C_{surf.}$) (φ=0.05, f=15 Hz, No of strokes=90).

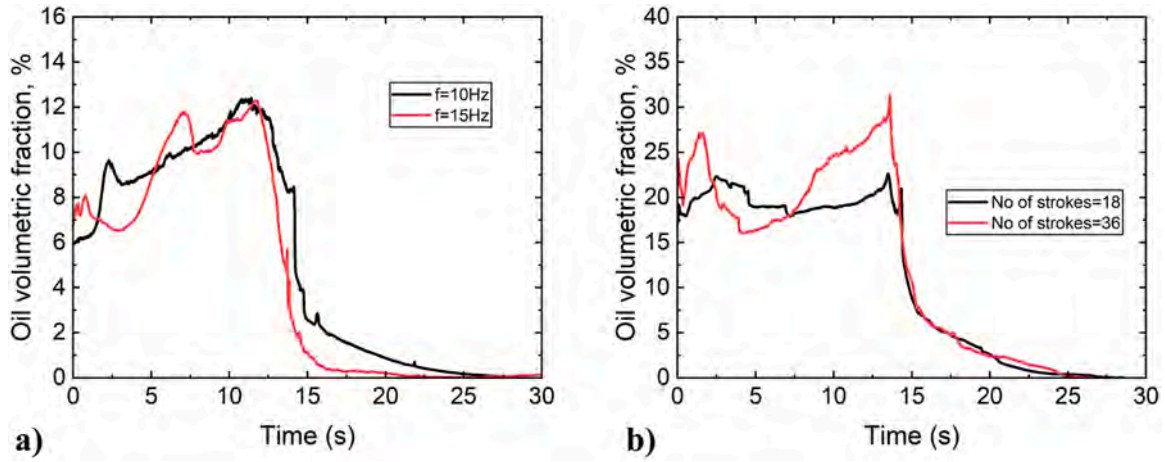


**Fig. 10.** Oil volumetric fraction evolution as a function of time during phase separation of emulsions with different **a)** pulsation stroke frequencies (f) (φ=0.1, $C_{surf.}$=2•10$^{-4}$ M, No of strokes=36) and **b)** number of strokes (φ=0.2, $C_{surf.}$=2•10$^{-4}$ M, f=15 Hz).

coefficient which is a function of Reynolds number Re based on the relative droplet-water velocity. The drag correlation of Feng and Michaelides [44] is selected since it accounts for the interaction between the viscous oil droplets and the less viscous carrier fluid. The correlation has two branches (see Eqs. 3a and 3b) depending on the value of the Reynolds number:

For Re < 5:

$$C_D = \frac{8}{\mathrm{Re}}\frac{3\lambda+2}{\lambda+1}\left(1+0.05\frac{3\lambda+2}{\lambda+1}\mathrm{Re}\right) - 0.01\frac{3\lambda+2}{\lambda+1}\mathrm{Re}\ln(\mathrm{Re}) \tag{3a}$$

For Re > 5 (and λ > 2):

$$C_D = \frac{68}{\lambda+2}\mathrm{Re}^{-2/3} + \left(\frac{\lambda-2}{\lambda+2}\right)\frac{24}{\mathrm{Re}}\left(1+\frac{1}{6}\mathrm{Re}^{2/3}\right) \tag{3b}$$

where λ is the viscosity ratio of oil to water. The above relation has been shown to hold for viscous drops up to 700 μm in diameter. In case of larger droplets deviation from the spherical shape may occur reducing the validity of the above equations. The steady state solution of Eq. 2 in the limit of small Reynolds is the Hadamard-Rubzinski [45] formula for the buoyancy velocity of the droplet.

In order to proceed, a discussion on the motion of water must be made. In order to keep the emulsion volume constant, water has to move in the opposite direction than the oil. The velocity of this motion is Vφ. So, the relative velocity between oil and water becomes U=V(1+φ). The Eq. 2 is non-linear and the derivation of the relaxation time of the particle motion is not straightforward. Instead, the relaxation time in the limit of small Reynolds number can be easily derived to be (see Eq. 4):

$$\tau = \frac{(\rho+0.5\rho_f)D^2 3(1+\lambda)}{18\mu(2+3\lambda)} \tag{4}$$

where D is the droplet diameter and μ is the water viscosity. The relaxation time even for droplets as large as D=0.5 mm does not exceed 0.02 s. This means that considering the rate of acceleration evolution (insignificant variation during the relaxation time) the motion of a droplet can be assumed to occur in pseudosteady conditions, i.e., the velocity is instantaneously adjusted to the current value of the induced acceleration α.

Up to now the discussion refers to the motion of an isolated droplet. However, the motion is hindered in the presence of other droplets due to the interaction between them. The effect of volume fraction φ of droplets on their motion has been extensively studied in literature. The most used expressions for this purpose are empirical ones like that of the Richardson-Zaki formula [46]. According to this, the drag force has to be multiplied by the term (see Eqs. 5 and 6):

$$K(\varphi) = (1-\varphi)^{-n} \tag{5}$$

$$n = \frac{1.791+0.133\mathrm{Re}^{0.456}}{0.359+0.093\mathrm{Re}^{0.456}} \tag{6}$$

It is noted that the above equation has been proposed for dispersed solid particles but the viscosity of the oil in the present work is about 30 times larger than that of water so the droplet hydrodynamic behavior is very close to that of a solid particle. Summarizing, the governing equations for the calculation of droplet velocity (see Eqs. 7 and 8) are:

$$\frac{3\rho}{8R}C_D[V(1+\varphi)]^2(1-\varphi)^{-n} = \left(\rho_f-\rho\right)g \tag{7}$$

$$\mathrm{Re} = \frac{\mathrm{V}(1+\varphi)\rho_f \mathrm{D}}{\mu} \tag{8}$$

Eqs. 3, 6, 7, 8 etc., constitute a nonlinear system of equations which must be solved numerically for the unknown velocity V. All the other variables result by simple substitution. In case of very small Reynolds number the above problem can be simplified to an analytical solution for the velocity given by Eq. 9:

$$V_o = \frac{2(\rho_f-\rho)\alpha(\lambda+1)(1-\varphi)^5}{3\mu(3\lambda+2)(1+\varphi)} \tag{9}$$

The effect of a finite Reynolds number can be shown through the ratio $V/V_o$. This ratio is presented in Fig. 11 as function of droplet diameter for several values of volume fraction φ. As expected, the velocity ratio is close to 1 for small Reynolds number. In case of an isolated droplet (φ=0), as droplet diameter increases, the increase of nonlinearity of the fluid dynamical problem leads to decrease of the velocity ratio. This decrease is smaller for φ=0.1. The reason is that K(φ) depends also on Reynolds and shows an increase as Reynolds increases. For φ=0.2 the effect of K(φ) increases, so the velocity ratio follows a non-monotonic behavior with respect to d.

The velocity ratio dependence on the induced acceleration α is shown in Fig. 12 for φ=0.1 and several droplet diameters. The ratio equals one for a droplet diameter of 100 μm and takes smaller values as d and/or g increases.

Let us now assume that all the droplets have the same size. This means that after the end of the micro-gravity region a front will be created at the cell separating the creamy phase from the aqueous water. The velocity of the front can be found at each moment in time by solving the system of Eqs. 3, 6, 7, 8 using the instantaneous value of α. The position of the front with respect to time can be found by numerically integrating in parallel the Eq. 10:

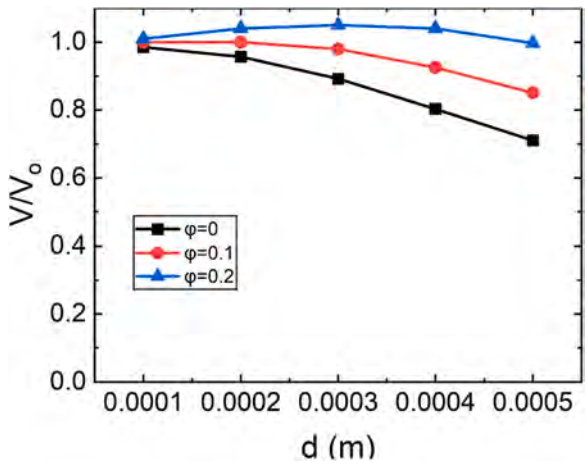


**Fig. 11.** The ratio $V/V_o$ versus droplet diameter for several values of oil volume fraction and terrestrial gravitational acceleration.

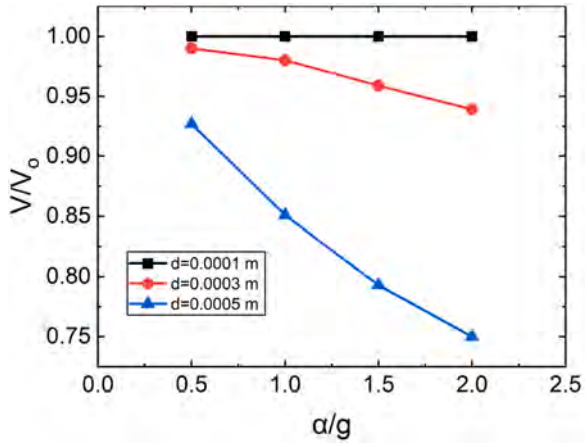


**Fig. 12.** The ratio $V/V_o$ versus imposed acceleration value α for several droplet diameters (φ=0.1).

$$\frac{dx}{dt} = V \tag{10}$$

where x is the distance from the bottom of the cell and x=0 at t=0. The motion of the front using a typical experimental curve of α (t) appears in Fig. 13. It is obvious that the motion intensifies as droplet diameter and oil fraction decrease. From such a position curve the time between the values of x corresponding to the position of the two electrodes can be computed and by comparing this time to the experimental time of transition $t_c$ between initial and zero oil fraction a characteristic droplet diameter can be found. The fact that the x curves after an initial delay are linear leads to a further simplification of the problem. The time $t_c$ is found from the oil fraction evolution curve. The average value of induced acceleration $\alpha_{av}$ during this time is calculated from the experimental induced acceleration data. Then the average velocity of the front is computed as $V_{av}=\Delta/t_c$ where Δ is the distance between the two electrodes. Finally, the system of Eqs. 3, 6, 7, 8 is solved using $V_{av}$ and $\alpha_{av}$ to calculate a characteristic droplet size $d_c$.

By observing the shape of the oil fraction curves, it is apparent that at most of the times the droplet size distribution can be approximated by a bidisperse rather than by a monodisperse one. There are two fronts, the one corresponding to larger droplets and the other to smaller droplets. The first corresponds to the first fast reduction of the oil fraction and the second to the second slower reduction. A time $t_s$ is selected for the transition from one front to the other and the corresponding value of

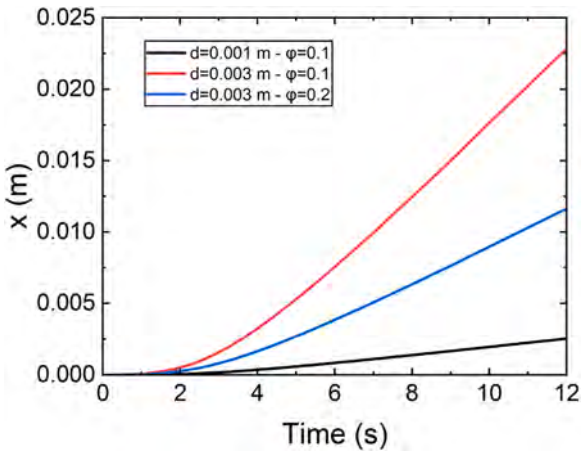


**Fig. 13.** Evolution of emulsion front position for monodisperse droplets, at terrestrial gravitational acceleration and several pairs of droplet diameter/oil fraction.

φ=$\varphi_c$ is calculated. In particular, in order to find the oil volumetric fraction $\varphi_c$ from an experimental curve the two different periods of time for the two fronts $\Delta t_1$ and $\Delta t_2$ are determined first. Afterwards, tangential lines at the two "linear" parts concerning these periods are drawn and their intersection point corresponding to an oil content $\varphi_c$ is estimated (Fig. 14). The average value of the induced acceleration is calculated from the experimental data for these periods of time. The procedure described above is applied separately for the two regimes (periods $\Delta t_1$ and $\Delta t_2$) leading to estimation of the size $d_l$, $d_s$ of both large and small droplets (Table 1) where $\varphi_c$ is the estimation of volume fraction of the small droplets. The parameters $\varepsilon_s=\varphi_c$ and $\varepsilon_l=\varphi-\varphi_c$ denoting the volume fraction of small and large droplets respectively, are also shown in Table 1.

It is necessary to make clear that the above proposed procedure does not imply that the droplet size distribution consists of two droplet sizes but that it can be simply characterized by two representative sizes. The electrical technique can in principle be used to derive the complete droplet size distribution under well defined conditions [31]. Here there are uncertainties regarding transverse uniformity of oil volume fraction and the bidisperse approximation (based on the shape of the electrical resistance curves) is the most informative choice that can be made. This is compatible to the mechanism of droplet breakage which suggests that breakage occurs in unequal fragment leading to a few large parent droplets and many small daughter droplets [47]. The above technique is

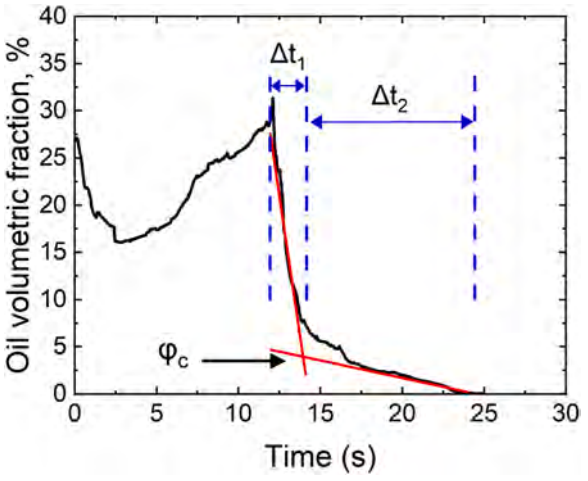


**Fig. 14.** The procedure followed in order to calculate the two slopes and the transition point $\varphi_c$.

**Table 1**
Results from the theoretical analysis of electrical data based on the assumption of a bidisperse droplet size distribution: droplet diameters $d_l$ and $d_s$ with oil volumetric fractions $\varepsilon_l$ and $\varepsilon_s$ respectively.

| φ | $C_{surf.}$ (M) | f (Hz) | No of strokes | $d_l$ (μm) | $\varepsilon_l$ | $d_s$ (μm) | $\varepsilon_s$ |
|---|---|---|---|---|---|---|---|
| 0.1 | $10^{-5}$ | 15 | 18 | 971 | 5.92 | 178 | 4.08 |
| 0.1 | $2\bullet10^{-4}$ | 10 | 18 | 512 | 7.43 | 152 | 2.57 |
| 0.1 | $10^{-5}$ | 10 | 36 | 1610 | 3.92 | 163 | 6.08 |
| 0.1 | $2\bullet10^{-4}$ | 10 | 36 | 586 | 7.11 | 142 | 2.89 |
| 0.1 | $2\bullet10^{-4}$ | 15 | 36 | 660 | 7.88 | 261 | 2.12 |
| 0.2 | $10^{-5}$ | 15 | 9 | 240 | 0.2 | - | - |
| 0.2 | $2\bullet10^{-4}$ | 15 | 18 | 250 | 11.9 | 180 | 8.10 |
| 0.2 | $2\bullet10^{-4}$ | 15 | 36 | 214 | 11.21 | 203 | 8.79 |
| 0.05 | $10^{-5}$ | 15 | 18 | 216 | 3 | 127 | 2 |
| 0.05 | $10^{-5}$ | 10 | 9 | 388 | 2.1 | 165 | 2.9 |
| 0.05 | $10^{-5}$ | 15 | 36 | 220 | 2.17 | 214 | 2.83 |
| 0.05 | $2\bullet10^{-4}$ | 15 | 36 | 656 | 3.05 | 214 | 1.95 |
| 0.05 | $10^{-5}$ | 15 | 90 | 1074 | 3.14 | 194 | 1.86 |
| 0.05 | $2\bullet10^{-4}$ | 15 | 90 | 713 | 3.53 | 155 | 1.47 |

based on the volumetric effect of droplets on the emulsion electrical resistance. In addition, the velocity of the front depends approximately on the droplet size squared so the average diameter calculated is of very large order and definitely not related in any way with the number based average diameter. The two methods are relevant to two different diameters namely the $D_{1,0}$ for image processing and the $D_{5,3}$ for the electrical technique. As it has been shown in the past [20] through examples the two diameters can be quite different for a broad size distribution. Actually they coincide for a monodisperse distribution and start to deviate from each other as the width of the distribution increases. Even the characteristic diameter of small droplets is weighted towards the larger sizes of this category. In some cases, appearing in Table 1, the large droplets diameter is of the order of 1 mm. Such a case implies that there is a single mass of oil escaping the breakage process. This situation cannot be observed by the image analysis method but it can be found by the electrical resistance evolution curve analysis. The domination of large sizes in the results of the electrical technique with the combination of the small number of the large droplets gives a rather stochastic nature to the outcome of the corresponding analysis. This leads to the fact that no specific trends at the sizes of the Table 1 with respect to the emulsification conditions can be drawn unlike the situation with the daughter droplets represented by the number-based average diameter.

## 5. Conclusions

A novel pulsation-based emulsification cell, along with advanced optical and electrical diagnostics are used to produce oil-in-water emulsions and provide information on their behavior at varying gravity conditions during parabolic flights. Both optical and electrical measurements proved for the first time that in the absence of gravity, the buoyancy related phenomena are eliminated and phase gravitational separation does not take place. Droplets motion and droplet-droplet interactions get slower and different coalescence events are observed between droplets of either the same or different sizes while coming in close contact from different directions. The employed electrical impedance spectroscopy technique was capable of registering non-intrusively the spatial distribution of volumetric oil fraction in the measuring region inside the experimental cell during ~0 g. With appropriate theoretical treatment the evolution of electrical signals at ~1.8 g are employed to estimate the two characteristic droplet sizes of an assumed bimodal distribution. These sizes are quite different from those obtained from optical observation and in particular, are shifted to much larger values. The explanation of this deviation is the different measuring principles of the two techniques corresponding to number-based and volume-based droplet size distributions. Better understanding of underlying phenomena (coalescence) by exploiting the simplified environment of micro-gravity is expected to improve the emulsification process for the production of more stable emulsions in industry. The effect of microgravity in emulsification process is not clear based solely on the findings of the present work. In order to identify this effect, experiments under the same conditions in absence and presence of gravity allowing a direct comparison between them will be performed in the future.

## CRediT authorship contribution statement

**Sotiris P. Evgenidis:** Methodology, Investigation, Data curation, Conceptualization. **Angeliki P. Chondrou:** Writing – original draft, Methodology, Investigation, Formal analysis, Data curation, Conceptualization. **Margaritis Kostoglou:** Writing – review & editing, Writing – original draft, Supervision, Methodology, Investigation, Data curation, Conceptualization. **Thodoris D. Karapantsios:** Writing – review & editing, Supervision, Project administration, Methodology, Investigation, Funding acquisition, Conceptualization.

## Declaration of Competing Interest

The authors declare that they have no known competing financial interests or personal relationships that could have appeared to influence the work reported in this paper.

## Data availability

Data will be made available on request.

## Acknowledgements

This study was funded by esa PRODEX Project: Dynamics of Emulsion Droplet Interactions in Low Gravity Conditions, Low-G-Emulsion – Contract No.: 4000132920. The view expressed herein can in no way be taken to reflect the official opinion of the European Space Agency.

## References

[1] P. Ahmadi, H. Asaadian, S. Kord, A. Khadivi, Investigation of the simultaneous chemicals influences to promote oil-in-water emulsions stability during enhanced oil recovery applications, J. Mol. Liq. 275 (2019) 57–70.
[2] M. Chappat, Some applications of emulsions, Colloids Surf. A: Physicochem. Eng. Asp. 91 (1994) 57–77.
[3] S. Hiranphinyophat, A. Otaka, Y. Asaumi, S. Fujii, Y. Iwasaki, Particle-stabilized oil-in-water emulsions as a platform for topical lipophilic drug delivery, Colloids Surf. 197 (2021) 111423.
[4] F. Leal-Calderon, V. Schmitt, J. Bibette, Emulsion Science: Basic Principles, 2nd Ed, Springer, USA, 2007.
[5] B.P. Binks, Cambridge. Modern Aspects of Emulsion Science, The Royal Society of Chemistry, 1998.
[6] L.L. Schramm, Emulsions, Foams and Suspensions, Fundamentals and Applications, Wiley-VCH Verlag GmbH & Co KGaA, Weinheim, Germany, 2005.
[7] T.F. Tadros, Emulsions Formation and Stability, Wiley-VCH, Weinheim, Germany, 2013.
[8] A. Williams, J.J.M. Janssen, A. Prins, Behaviour of droplets in simple shear flow in the presence of a protein emulsifier, Colloids Surf. A: Physicochem. Eng. Asp. 125 (1997) 189–200.
[9] M.J. Rosen. Surfactants and interfacial phenomena, 3rd Ed., John Wiley & Sons Inc, New Jersey, USA, 2004.
[10] R.J. Farn, Chemistry and Technology of Surfactants, Wiley-Black, UK, 2006.
[11] W. Zhang, Y. Zhang, Y. He, X. Xu, X. Zhao, Oil density and viscosity affect emulsion stability and destabilization mechanism, J. Food Eng. 366 (2024) 111864.
[12] M.J.J. Janssen, A. Boon, M.W.G. Agterof, Droplet break-up in simple shear flow in the presence of emulsifiers, Colloids Surf. A: Physicochem. Eng. Asp. 91 (1994) 141–148.
[13] M. Antoni, J. Kragel, L. Liggieri, R. Miller, A. Sanfeld, J.D. Sylvain, Binary emulsion investigation by optical tomographic microscopy for FASES experiments, Colloids Surf. A: Physicochem. Eng. Asp. 309 (2007) 280–285.
[14] J. Banhart, F. Garcia-Moreno, S. Hutzler, D. Langevin, L. Liggieri, M. Reinhard, A. Saint Jalmes, D. Weaire, Foams and emulsions in space, Europhys. News 39 (2008) 26–28.

[15] M.I.I.Z. Abidin, A.A.A. Raman, M.I.M. Nor, Review on measurement techniques for drop size distribution in a stirred vessel, Ind. Eng. Chem. Res. 52 (46) (2013) 16085–16094.
[16] D.J. McClements, Food Emulsions: Principles, Practices and Techniques. 2nd Ed, CRC Press, Florida, 2005.
[17] D. Orsi, F. Salerni, E. Macaluso, E. Santini, F. Ravera, L. Liggieri, L. Cristofolini, Diffusing wave spectroscopy for investigating emulsions, Colloids Surf. A: Physicochem. Eng. Asp. 580 (2019) 123574.
[18] F. Salerni, D. Orsi, E. Santini, L. Liggieri, F. Ravera, L. Cristofolini, Diffusing wave spectroscopy for investigating emulsions: II. Characterization of a paradigmatic oil-in-water emulsion, Colloids Surf. A: Physicochem. Eng. Asp. 580 (2019) 123724.
[19] V. Lorusso, D. Orsi, F. Salerni, L. Liggieri, F. Ravera, R. McMillin, J. Ferri, L. Cristofolini, Recent developments in emulsion characterization: Diffusing Wave Spectroscopy beyond average values, Adv. Colloid Interface Sci. 288 (2021) 102341.
[20] M. Kostoglou, E.M. Varka, E.P. Kalogianni, T.D. Karapantsios, Evolution of volume fractions and droplet sizes by analysis of electrical conductance curves during destabilization of oil-in-water emulsions, J. Colloid Interface Sci. 349 (1) (2010) 408–416.
[21] A.P. Chondrou, S.P. Evgenidis, K.A. Zacharias, M. Kostoglou, T.D. Karapantsios, Development of an Experimental Device for the Assessment of Emulsions Dynamic Behavior and Stability in Micro-gravity, Microgravity Sci. Technol. 35 (2023) 28.
[22] X. Zabulis, M. Papara, A. Chatziargyriou, T.D. Karapantsios, Detection of densely dispersed spherical bubbles in digital images based on a template matching technique. Application to wet foams, Colloids Surf. A: Physicochem. Eng. Asp. 309 (1-3) (2007) 96–106.
[23] S.P. Evgenidis, T.D. Karapantsios, Effect of bubble size on void fraction fluctuations in dispersed bubble flows, Int. J. Multiph. Flow. 75 (2015) 163–173.
[24] S.P. Evgenidis, T.D. Karapantsios, Pulsatile gas-liquid flow resembling Decompression Sickness: Computational Fluid Dynamics simulation and experimental validation, Int. Marit. Health 73 (4) (2022) 189–198.
[25] S. Evgenidis, A. Chondrou, T. Karapantsios, A new phantom that simulates electrically a human blood vessel surrounded by tissues: Development and validation against in-vivo measurements, Ann. Biomed. Eng. 6 (2023) 1284–1295.
[26] P.K. Gkotsis, S.P. Evgenidis, T.D. Karapantsios, Influence of Newtonian and non-Newtonian fluid behavior on void fraction and bubble size for a gas-liquid flow of sub-millimeter bubbles at low void fractions, Exp. Therm. Fluid Sci. 109 (2019) 109912.
[27] P.K. Gkotsis, S.P. Evgenidis, T.D. Karapantsios, Associating void fraction signals with bubble clusters features in co-current, upward gas-liquid flow of a non-Newtonian liquid, Int. J. Multiph. Flow. 131 (2020) 103297.
[28] O. Oikonomidou, S.P. Evgenidis, M. Kostoglou, T.D. Karapantsios, Degassing of a pressurized liquid saturated with dissolved gas when injected to a low pressure liquid pool, Exp. Therm. Fluid Sci. 96 (2018) 347–357.
[29] O. Oikonomidou, S.P. Evgenidis, C.J. Schwarz, W.A. van Loon J. J, M. Kostoglou, T. D. Karapantsios, Degassing of a decompressed flowing liquid under hypergravity conditions, Int. J. Multiph. Flow. 115 (2019) 126–136.
[30] W. Tzevelekos, Q. Galand, S. Evgenidis, K. Zacharias, T.D. Karapantsios, S. Vaerenbergh, High-resolution concentration measurement in water/n-butanol binary system by means of high-frequency electrical impedance method, Exp. Therm. Fluid Sci. 126 (2021) 110399.
[31] M.C. Vlachou, K.A. Zacharias, M. Kostoglou, T.D. Karapantsios, Droplet size distributions derived from evolution of oil fraction during phase separation of oil-in-water emulsions tracked by electrical impedance spectroscopy, Colloids Surf. A: Physicochem. Eng. Asp. 586 (2020) 124292.
[32] A.P. Chondrou, T.D. Karapantsios, M. Kostoglou, Effect of width/height of the gap between piston and wall on the performance of a novel small volume emulsification device, Colloids Surf. A: Physicochem. Eng. Asp. 126 (2021) 126702.
[33] F. Risso, The mechanisms of deformation and breakup of drops and bubbles, Multiph. Sci. Technol. 12 (2000) 1–50.
[34] A.H. Kori, S.A. Mahesar, S.T.H. Sherazi, U.A. Khatri, Z.H. Laghari, T. Panhwar, Effect of process parameters on emulsion stability and droplet size of pomegranate oil-in-water, Grasas Aceites 72 (2021) 2.
[35] S.K. Naeeni, L. Pakzad, Droplet size distribution and mixing hydrodynamics in a liquid-liquid stirred tank by CFD modeling, Int. J. Multiph. Flow. 120 (2019) 103100.
[36] L.N.M. Suli, A.H. Nour, D. Rizauddin, J. Gimbun, S. Nurdin, Stabilization and Characterization of Heavy Crude Oil in Water (O/W) Emulsions, IJRET 3 (2) (2014) 489–496.
[37] A. Sielaff, J. Dietl, S. Herbert, P. Stephan, The influence of system pressure on bubble coalescence in nucleate boiling, Heat. Transf. Eng. 35 (5) (2014) 420–429.
[38] A.B. Basset, Treatise on Hydrodynamics, Bell & Co, London, 1888.
[39] C.M. Tchen, Mean values and correlation problems connected with the motion of small particles suspended in a turbulent fluid, Doctoral Dissertation, Delft, 1949.
[40] M.R. Maxey, J.J. Riley, Equation of motion for a small rigid sphere in a non-uniform flow, Phys. Fluids 26 (4) (1983) 883–889.
[41] E.E. Michaelides, Particles, bubbles and drops; Their motion, heat and mass transfer, World Scientific, New Jersey, 2006.
[42] M.R. Snyder, O.M. Knio, J. Katz, O.P. Le Maitre, Numerical study on the motion of microscopic oil droplets in high intensity isotropic turbulence, Phys. Fluids 20 (2008) 073301.
[43] M.R. Snyder, O.M. Knio, J. Katz, O.P. Le, Maitre, Statistical analysis of small bubble dynamics in isotropic turbulence, Phys. Fluids 19 (2007) 065108.
[44] Z.G. Feng, E.E. Michaelides, Drag coefficients of viscous spheres at intermediate and high Reynolds numbers, ASME, J. Fluids Eng. 123 (2001) 841–849.
[45] R.S. Subramanian, R. Balasubramanian, The motion of bubbles and drops in reduced gravity, Cambridge University Press, New York, 2001.
[46] A.V. Nguyen, H.J. Schulze, Colloidal Science of Flotation, Marcel Decker, New York, 2004.
[47] M. Kostoglou, A.J. Karabelas, Towards a unified framework for the derivation of breakage functions based on the statistical theory of turbulence, Chem. Eng. Sci. 60 (2005) 6584–6595.